Multiple Objective Co-Optimization and Experimental Evaluation of Switched Reluctance Machine Design and Control

Timothy Burress
Oak Ridge National Laboratory
burressta@ornl.gov

Leon M. Tolbert
The University of Tennessee
tolbert@utk.edu

2023 IEEE International Electric Machines & Drives Conference (IEMDC) | 979-8-3503-9899-1/23/$31.00 ©2023 IEEE | DOI: 10.1109/IEMDC55163.2023.10238900

***Abstract*—A new modeling framework and optimization approach is proposed for co-optimization of both switched reluctance machine (SRM) design and control across the entire torque-speed range. Custom modeling codes use static finite element analysis (FEA) results to determine optimal current profiles and conventional control conditions for discrete speeds, torques, and torque ripple levels. A machine design optimization method is proposed that leverages outputs from control optimization and determines quality metrics for each design based on the efficiency and torque ripple across the operation envelope. Simulations are validated through empirical testing across the entire torque-speed operation range as comparisons of transient FEA, custom models, and tests are presented.**

***Keywords*—Switched reluctance machine, machine design and control optimization**

I. Introduction

Switched reluctance machines (SRMs) have low material and manufacturing costs that have led to their use in many applications [1]. However, their inherent torque ripple, acoustic noise, and atypical control have hindered their adoption in other applications. Torque ripple and acoustic noise characteristics are largely driven by both the SRM geometry and control method. Modeling of SRM operation is challenging due to the magnetically salient stator and rotor members which lead to nonlinear magnetic behavior with respect to both position and current.

Simulation of SRMs with electromagnetic FEA software is the most accurate modeling method, and FEA results are therefore often used as a reference to determine the quality and effectiveness of alternative modeling methods. The FEA modeling environment is flexible with the ability to easily parameterize various geometric features and winding characteristics, and the approach is well established for many electromagnetic and multi-physics problems, in general. Due to the high computational demand of transient FEA simulations in the time domain, most broad FEA-based parameter optimization in the literature relies on static FEA.

Multi-objective optimization of SRM design parameters using static FEA results with evolutionary algorithms is presented in [2]. Some researchers focus specifically on tooth shape optimization based on torque results from magnetostatic FEA [3]. A common technique used to model transient behavior without the computational expense of transient FEA is the of use circuit equations that rely on flux linkage and torque mapping from static FEA simulations [4-5]. Primary alternatives to FEA based optimization include magnetic equivalent circuit modeling [6-7] and other analytical techniques [8-9]. These analytical methods are often used to develop closed-form solutions that greatly facilitate optimization of a wide range of design parameters without the need for iterative time-domain simulations [10]. Design optimization has been demonstrated with a wide range of algorithms including particle swarm optimization [11], genetic algorithms [2,10], and differential evolution [12]. Overall, it is generally acknowledged that there is a trade-off between the accuracy of FEA-based methods versus computational efficiency of analytical-based methods [13].

The most widely used conventional control method for SRMs is hysteresis current control, where lookup tables and/or functions define on/off angles and current magnitudes that determine how and when the hysteresis-band current regulator operates. One torque ripple mitigation control technique involves current profiling, where a specific irregular current reference waveform is defined versus position [14-16]. This is often implemented with lookup tables that define current profiles at various points in the torque-speed operation range. This method is effective particularly for low and moderate speeds but may encounter limitations at high speeds depending on various machine and system characteristics. Other control methodologies such as torque sharing functions (TSFs) [17], direct torque control [18], flux observers [19], fuzzy logic [20], advanced neural networks, and sliding mode controllers [21] aim to offer more simple solutions for torque ripple minimization.

With a few exceptions, the control methods mentioned above are implemented in the time domain, and typically are not implemented alongside broad FEA-based parametric optimization. Closed-form analytical SRM modeling solutions offer the ability to account for operational impacts without time domain modeling, yet they often lack the accuracy and flexibility of FEA-based models. Most analytical models developed for conventional geometric configurations may not suffice for wide-ranging parametric sweeps, detailed tooth shape optimization, leveraging of beneficial mutual coupling [5], and unconventional stator-rotor pole configurations and excitation schemes.

This paper proposes and demonstrates the advantages of an approach for co-optimization of both SRM design and control using static FEA-based machine models with custom voltage fed machine models for optimization with respect to voltage and other system parameters throughout the torque-speed operation region.

II. Proposed Modeling and Optimization Framework

The proposed modeling and optimization framework, described in [22] includes FEA-based machine modeling while addressing computational constraints of transient FEA. It involves the use of magnetostatic FEA to map flux linkage and torque as a function of current and rotor position. Partial derivatives of the flux linkage with respect to current and position are implemented in the voltage equation to determine dynamic operation of the SRM:

$$\begin{bmatrix} v_a \\ v_b \\ v_c \end{bmatrix} = R \begin{bmatrix} i_a \\ i_b \\ i_c \end{bmatrix} + \begin{bmatrix} \frac{\partial \psi_a}{\partial i_a} & \frac{\partial \psi_a}{\partial i_b} & \frac{\partial \psi_a}{\partial i_c} \\ \frac{\partial \psi_b}{\partial i_a} & \frac{\partial \psi_b}{\partial i_b} & \frac{\partial \psi_b}{\partial i_c} \\ \frac{\partial \psi_c}{\partial i_a} & \frac{\partial \psi_c}{\partial i_b} & \frac{\partial \psi_c}{\partial i_c} \end{bmatrix} \frac{d}{dt} \begin{bmatrix} i_a \\ i_b \\ i_c \end{bmatrix} + \begin{bmatrix} \frac{\partial \psi_a}{\partial \theta} \\ \frac{\partial \psi_b}{\partial \theta} \\ \frac{\partial \psi_c}{\partial \theta} \end{bmatrix} \omega \quad (1)$$

Code-based voltage fed and steady state current fed machine models were developed to perform dynamic simulations using outputs from magnetostatic FEA. Machine design optimization is based on output from current fed and voltage fed models where the maximum torque envelope, efficiency, torque ripple, and other operational characteristics are determined across the torque-speed operation region with consideration of voltage limits. The code-based models greatly facilitate the implementation of comprehensive control optimization as hundreds of control conditions can be simulated in the time it takes to simulate one condition with 2D transient FEA.

III. Proposed Machine Design Optimization Process

A three-stage machine design optimization process is shown in the diagram in Fig. 1. Since detailed simulations require time-intensive mapping of each machine at many currents and positions, the first two stages are used to down-select from a wide range of designs to a reduced solution space.

First, a base design is selected and features are identified for parameterization. An initial solution space is determined by selecting a nominal range of values for each parameter, and magnetostatic FEA is used to generate mappings of flux, torque, and other parameters for various combinations of rotor positions and three-phase currents (to account for mutual coupling). Stage 1 involves relatively coarse mapping with only 1-3 currents over the positive torque production range to allow for broad sweeps of geometrics parameters. The performance of each solution (defined as set of geometric parameters) is determined by evaluating zero speed capabilities such as peak and continuous average torque, and the ratio of torque to current density. The solution space is expanded as needed based on evaluations of performance and performance-parameter sensitivity. The large solution space in Stage 1 is significantly reduced as leading geometries are selected for Stage 2 based on Stage 1 performance function results.

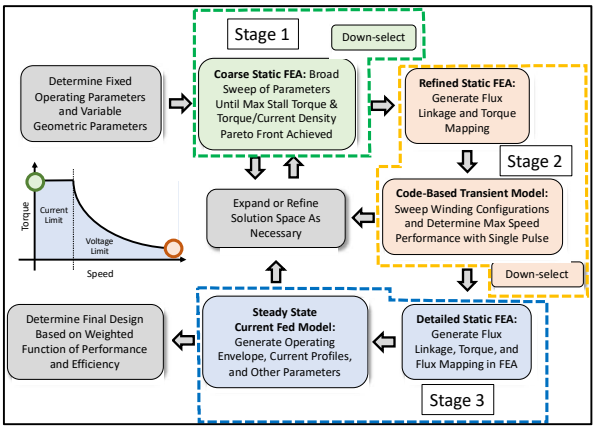

Fig. 1. Proposed SR machine design optimization process.

Stage 2 simulations entail more detailed static FEA mapping of torque and flux linkage and involve transient simulations under maximum power and speed conditions to further reduce the solution space while performance metrics such as operational efficiency and torque ripple are evaluated. Simulations in Stage 1 and Stage 2 play an important role in defining and reducing the solution space as it relates to winding parameters such as the wire size and the number of strands, turns, and coils in parallel. For a given machine, winding parameter variations result in a trade-off between achieving maximum torque at low speeds versus maximum power at high speeds, which is largely limited by the winding impedance and pseudo back-EMF.

High power density traction machines typically operate in or near the voltage limited condition at maximum power and speed and therefore the applied voltage is often limited to a single pulse waveform. This reduces the number of control conditions to be swept, and the solution space is greatly reduced before detailed transient simulations and control optimization is performed throughout the torque-speed range in Stage 3. Optimal control conditions are selected at each torque-speed point based on performance function evaluations and weighting factors applied to operational metrics such as efficiency versus torque ripple, with torque ripple defined as:

$$\tau_{ripple} = (\tau_{max} - \tau_{min})/(2\,\tau_{average}) \quad (2)$$

After control optimization is completed in Stage 3, the value of each machine is determined by a performance function evaluating operational metrics such as efficiency and torque ripple at various points throughout the torque-speed range.

The solution space is expanded as necessary in Stages 2 and 3 based on machine performance values, and new points in the solution space may need to be identified by using an evolutionary algorithm such as particle swarm optimization if the number of design parameters is high or if machine performance function is complex.

IV. Exemplar Design and Control Optimization Using Proposed Approach

A. Nominal Design Parameters

The Nissan LEAF primary traction drive electric machine was selected as a baseline reference since detailed design, performance, and operational metrics are publicly available [23]. The goal of this example is to demonstrate how the proposed approach can be implemented, and not necessarily match the performance and efficiency of reference design. Based on design and operational parameters of the LEAF electric machine, fixed parameters throughout the optimization process include a targeted rated power of 80 kW, rated torque of 280 Nm, maximum speed of 10,000 rpm, DC link voltage of 375 Vdc, an air gap of 0.5 mm, and a stator outer diameter of 200 mm. Nominal and potentially variable parameters include a rated phase current of 450 Arms, and a stack length of 151 mm. A nominal current density of 9 Arms per mm^2 was selected with the LEAF as a basis. This target is in the middle of the range of typical current density values (6-

14 Arms per mm^2) found in in water jacket-based cooling systems [24].

An SRM with 12 stator teeth and 8 rotor teeth, referred to as a '12-8' design, was selected since it is a 3-phase machine that can be driven by three switching devices and three diodes, similar to, but in a different arrangement, than that of conventional three-phase drive. Further, the number of rotor teeth was selected as a compromise between the effective high torque ripple associated with smaller numbers of rotor teeth, and the high operational frequencies and losses associated with higher numbers of rotor teeth.

The five geometric parameters shown in Fig. 2 were identified for an exemplar optimization exercise. The stator outer diameter (OD) is fixed at 200 mm, while the stator inner diameter (ID) varies based on the rotor OD and a fixed air gap of 0.5 mm. Stator yoke width, w_{Syoke}, and stator ID, D_{SI}, determines the depth of stator slots. Rotor tooth length, l_{Rtooth}, determines the length of the rotor tooth between the OD of the rotor back-iron and rotor OD, D_{RO}. Widths of stator and rotor teeth are determined by the stator and rotor tooth width factors according to

$$w_{ST} = D_{SI}\frac{\pi}{N_S}\frac{1}{2}k_{STW} \tag{3}$$

$$w_{RT} = D_{RO}\frac{\pi}{N_S}\frac{1}{2}k_{RTW} \tag{4}$$

where w_{ST} is the stator tooth width, N_S is the number of stator teeth, k_{STW} is the stator tooth width factor, w_{RT} is the rotor tooth width, and k_{RTW} is the rotor tooth width factor. With the exception of k_{RTW}, all other parameters impact the cross-sectional area available in the stator slot for windings and this was considered in the calculation of winding parameters and various performance metrics.

The appropriate number of turns, N_{turns}, and strands, $N_{strands}$, based on an assumed slot fill factor, FF, a given wire cross-sectional area, A_{wire}, coil cross-sectional area, A_{coil}, number of parallel branches in a phase, N_{par}, targeted nominal current density, J_0, and phase current rating, I_{ph} were determined by:

$$N_{strands} = nearest\left(\frac{I_{ph}\,FF}{A_{wire}\,J_0\,N_{par}}\right) \tag{5}$$

$$N_{turns} = nearest\left(\frac{J_0\,A_{coil}N_{par}}{I_{ph}}\right) \tag{6}$$

where values for $N_{strands}$ and N_{turns} are the nearest integer of the ratio defined in parentheses.

Conventional stators wound with stranded wire typically have a fill factor in the range of 0.25 to 0.6. Wire cross-sectional area, A_{wire}, is determined by the gauge of wire and coil cross-sectional area, A_{coil}, is determined by area available in the slot for a coil. The 12-8 SRM analyzed in this example has a total of four coils per phase, therefore N_{par} can be 1, 2, or 4. The targeted nominal current density correlates with the anticipated losses and selected cooling approach, and phase current rating may be selected based on thermal limitations of the SRM or the current rating of the devices in the motor drive.

B. Stage 1 Simulations and Down-Selection

For this example, static electromagnetic FEA was conducted with over 900 geometry combinations across positions associated with positive torque at excitation levels of 2000 Amp-Turns (A-T) and 5000 A-T, which correlates with the steel operating at a point below and above the knee of the B-H curve, respectively. An initial solution space was identified with D_{RO} ranging from 110-140 mm, w_{Syoke} ranging from 9-19 mm, k_{STW} ranging from 0.9-1.2, k_{RTW} ranging from 0.8-1.2, and l_{Rtooth} ranging from 10-30 mm.

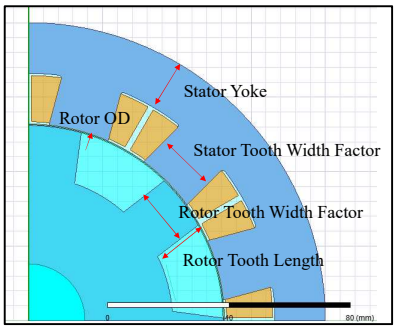

Fig. 2. Geometric parameters selected for exemplar optimization.

For each current level, the torque was averaged with respect to position, and the torque-current density (TCD) ratio was computed. The scatter plot in Fig. 3 is a plot of TCD ratio versus average torque at an excitation level of 5,000 A-T for the geometries simulated in Stage 1. The TCD ratio correlates with the thermal aspects of the machine, where higher values indicate a given torque can be produced with less resistive heat loss versus designs with lower TCD ratios. In general, designs with larger stator members and therefore smaller slot area result in higher average torque but lower TCD ratio for a given current. Conversely, designs with more slot area and small stator members trend toward higher TCD ratios and lower average torque. A performance function was used to determine the value of each design and after iterative expansion of the solution space, down-selected geometries were identified and are indicated with red circles.

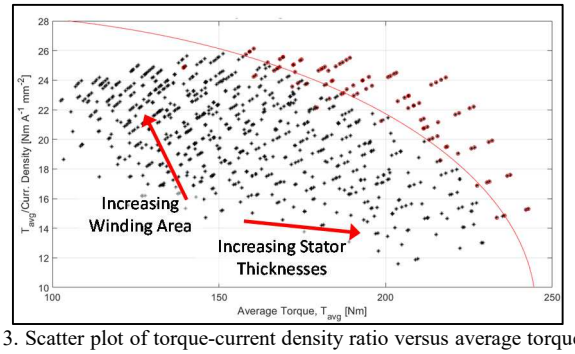

Fig. 3. Scatter plot of torque-current density ratio versus average torque for 5,000 A-T with down-selected geometries identified with red circles.

C. Stage 2 and 3 Simulations and Down-Selections

Stage 2 simulations rely on the voltage fed model to determine operational metrics at maximum speed, and the waveforms shown in Figs. 4 and 5 provide a comparison of transient FEA and the proposed code-based voltage fed model, respectively, at the maximum speed operation point using the same control conditions. While winding resistance loss calculations are straightforward, core losses were approximated by developing expressions for stator back-iron, stator tooth, rotor back-iron, and rotor tooth flux density as a function of flux-linkage and the time domain core loss equations described in [25] were implemented.

Comparing results of FEA and the voltage fed model, the average torque is 158 Nm and 160 Nm, the torque ripple is 49.3% and 48.9%, and the efficiency is 76.0 and 74.2%, respectively. Close agreement with transient FEA was achieved across the entire torque-speed region. Using a mid-performance desktop PC, transient FEA solve times ranged

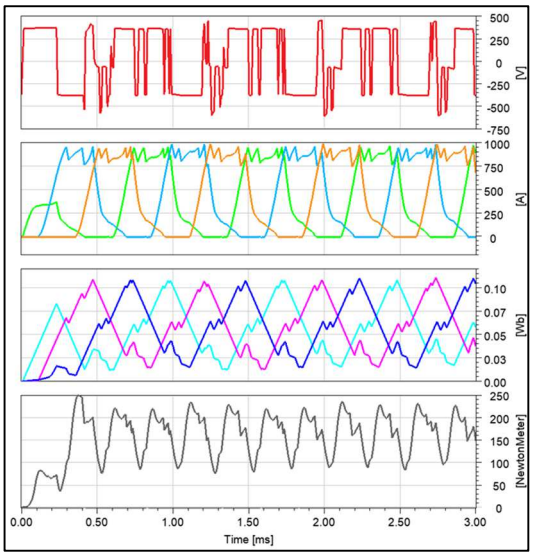

Fig. 4. Phase 'a' voltage, three-phase currents, three-phase flux-linkages, and torque waveforms from FEA transient simulations at 10,000 rpm.

from ~1-3 minutes per point with 16 cores while the voltage fed model solve time ranged from 0.5-3 seconds with a single core. Machine mapping with magnetostatic FEA consumed about 2 hours for Stage 2 and 6 hours for Stage 3. The short solve time greatly facilitates comprehensive optimization of control conditions throughout the torque-speed range.

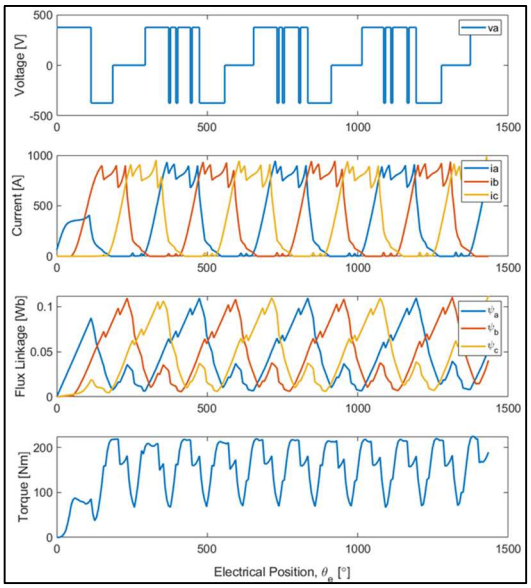

Fig. 5. Phase 'a' voltage, three-phase currents, three-phase flux-linkages, and torque waveforms from code-based voltage-fed simulations at 10,000 rpm.

For Stage 2 simulations at maximum speed, torque, efficiency, and torque ripple were determined as various types of single pulses were applied to the windings. Using conventional SRM control terminology, the advance angle, θ_a, is the amount of angular advance of the phase turn-on state (or the rising edge of the pulse in this case) with respect to the aligned condition of the stator and rotor teeth, and the dwell angle, θ_d, is the angular duration over which the phase is in the on-state.

Similar down-selection methods were used for Stages 2 and 3, as for any control method, the impact of various control conditions can be visualized by plotting efficiency versus torque ripple, such as in Fig. 6, where the plot includes results from various combinations of θ_a and θ_d that produce 7 N-m for each given reference current. The 7 N-m control conditions

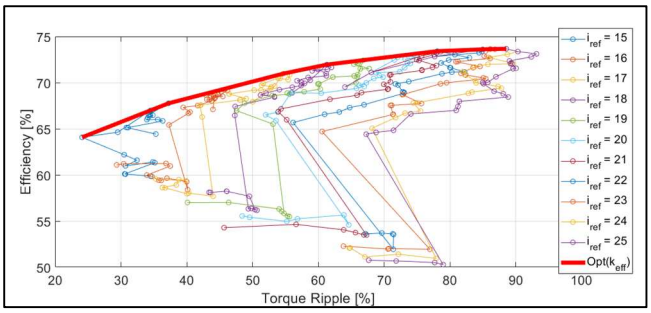

Fig. 6. Efficiency versus torque ripple for various reference currents and a torque of 7 N-m.

were determined (in Stage 3 simulations with conventional control) by sweeping θ_a and θ_d at a given speed and reference current, then interpolating the resulting map for each targeted torque level. Stage 2 conditions are similar but have only one reference current (maximum current) and rely on more coarse torque and flux linkage maps from static FEA.

A performance function can be used to determine which control conditions to use at each operation point. For this example, a simple performance function to determine the value of various control parameters was defined as

$$P_{ctrl} = k_{eff-ctrl}\,\overline{\eta} + \left(1 - k_{eff-ctrl}\right)\left(1 - \overline{\tau_{ripple}}\right) \quad (7)$$

where $\overline{\eta}$ and $\overline{\tau_{ripple}}$ are efficiency and torque ripple arrays normalized with respect to the all control conditions at each torque-speed point, and $k_{eff-ctrl}$ is a weighting factor varying from 0 to 1, with 0 correlating with full prioritization of torque ripple minimization and 1 correlating with full prioritization of efficiency maximization. The red trace in Fig. 6 indicates the optimal efficiency and torque ripple relationship determined by evaluating the performance function as $k_{eff-ctrl}$ ranges from 0 to 1. Therefore, control conditions can be selected based on the evaluation of the performance function at each operation point as $k_{eff-ctrl}$ is selected based on requirements of the application. To determine the value of each geometry across multiple points in the torque-speed plane, a performance function such as the following can be defined:

$$\begin{aligned} P_{TS} = {} & k_{eff-TS_1}\,\overline{\eta_1} + \left(1 - k_{eff-TS_1}\right)\left(1 - \overline{\tau_{ripple_1}}\right) + \\ & k_{eff-TS_2}\,\overline{\eta_2} + \left(1 - k_{eff-TS_2}\right)\left(1 - \overline{\tau_{ripple_2}}\right) + \ldots \\ & k_{eff-TS_m}\,\overline{\eta_m} + \left(1 - k_{eff-TS_m}\right)\left(1 - \overline{\tau_{ripple_m}}\right) \end{aligned} \quad (8)$$

where $\overline{\eta_{\mathrm{p=1\to m}}}$ and $\overline{\tau_{ripple}}_{\mathrm{p=1\to m}}$ are efficiency and torque ripple arrays normalized with respect to all geometries at each torque-speed point, p, and $k_{eff-TS}{}_{\mathrm{p=1\to m}}$ are weighting factors ranging from 0 to 1, with $k_{eff-TS_p} = 0$ correlating with full prioritization of torque ripple minimization and $k_{eff-TS_p} = 1$ correlating with full prioritization of efficiency maximization.

The weighting factor can be selected based on the importance of torque ripple or efficiency in different areas of the torque-speed range. For example, torque ripple minimization is more important for low speeds as vibrations can be felt more easily by the passenger, whereas torque ripple minimization at higher speeds is less important due to natural inertia related damping and road vibration.

For demonstration purposes, down-selections in Stage 2 were performed using three combinations of $k_{eff-ctrl}$ = k_{eff-TS} = 0, 0.5, and 1. As a part of Stage 3, the resulting three geometry solutions were simulated with the voltage fed model with detailed torque and flux-linkage mapping from 2D FEA as control parameters were swept at each torque-speed point to generate a full mapping of efficiency and torque ripple. Efficiency contour plots shown in Figs. 7 and 8 correlate with $k_{eff-ctrl}$ = 0 and 1, respectively, as the performance equation (7) was maximized at each point throughout the entire torque-speed range. Similarly, torque ripple contour plots in Figs. 9 and 10 correlate with $k_{eff-ctrl}$ = 0 and 1 throughout the entire torque-speed range, respectively.

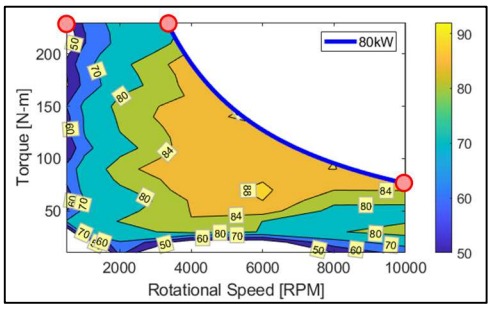

Fig. 7. Contours of simulated efficiency [%] plotted for torque versus speed for geometry index 2 with $k_{eff-ctrl}$ = 0.

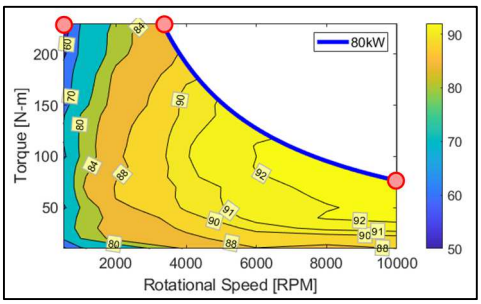

Fig. 8. Contours of simulated efficiency [%] plotted for torque versus speed for geometry index 2 with $k_{eff-ctrl}$ = 1.

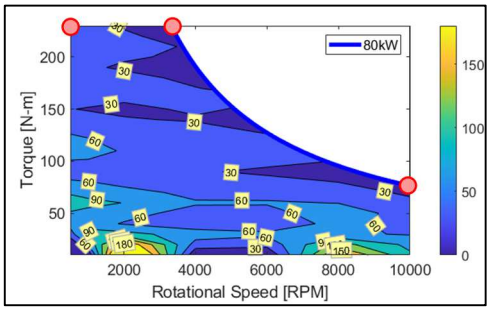

Fig. 9. Contours of simulated torque ripple [%] plotted for torque versus for geometry index 2 speed with $k_{eff-ctrl}$ = 0.

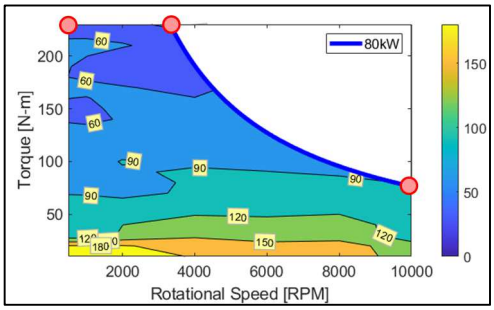

Fig. 10. Contours of simulated torque ripple [%] plotted for torque versus for geometry index 2 speed with $k_{eff-ctrl}$ = 1.

Efficiency and torque ripple for all three geometries at the 500 rpm, 230 Nm operation point (indicated by one of the red circles in the contour plots) is shown in Figs. 11(a) and 11(b), respectively, for $k_{eff-ctrl}$ = 0, 0.5, and 1. For almost all control conditions, efficiency is maximized and torque ripple is minimized with geometry 2. Analogous to what is indicated in Fig. 3, geometry 1 is a machine with more winding area, geometry 3 is a machine with less winding area and thicker iron segments, while geometry 2 is a compromise between the two. The torque-speed performance equation (8) was implemented while including all three points indicated by red circles on the contour plot and the resulting performance of all three geometries is plotted versus k_{eff-TS} for $k_{eff-ctrl}$ = 0, 0.5, and 1, in Figs. 12(a), 12(b), and 12(c), respectively. With the exception of a few conditions, it can be seen that the evaluated value of geometry 2 is greater than that of the other geometries. This example demonstrates how the proposed framework can be used to achieve co-optimization of both machine and control conditions.

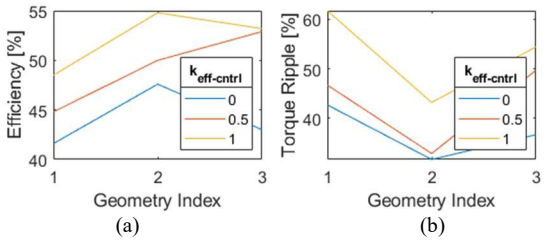

Fig. 11. Simulated efficiency (a) and torque ripple (b) of three geometries at 500 rpm and 230 N-m for various control weighting factors, $k_{eff-ctrl}$.

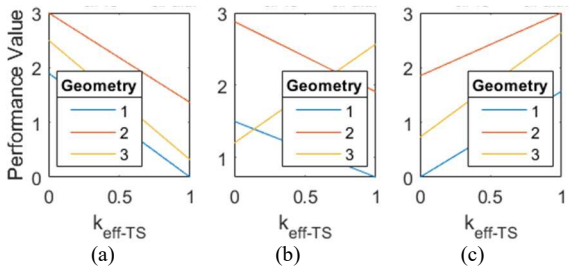

Fig. 12. Machine performance versus k_{eff-TS} for three geometries with $k_{eff-ctrl}$ = 0 (a), 0.5 (b), and 1 (c).

V. Experimental Validations

The final optimal solution (geometry 2) in the example above correlates with D_{RO} = 130 mm, w_{Syoke} = 11 mm, k_{STW} = 1.1, k_{RTW} = 1.1, and l_{Rtooth} = 20 mm. In preparation for empirical validations, the geometry was scaled to a 5 hp (3.7 kW) power level and scaled parameter values are D_{RO} = 83.1 mm, w_{Syoke} = 7 mm, k_{STW} = 1.1, k_{RTW} = 1.1, and l_{Rtooth} = 13 mm. Other parameter changes include the reduction of the stator OD from 200 mm to 127.91 mm, rotor OD from 130 mm to 83.14 mm, stator/rotor stack length from 196.3 mm to 76.2 mm. A prototype SRM (Fig. 13) was fabricated, assembled, and installed on a dynameter test setup (Fig. 14). The housing, bearing system, and resolver position feedback sensor of a Hyundai Sonata hybrid starter-generator was used. A custom SRM drive was fabricated by modifying two conventional 3-phase power stages, programming a DSP/microcontroller, and implementing proper signal conditioning for current and position feedback.

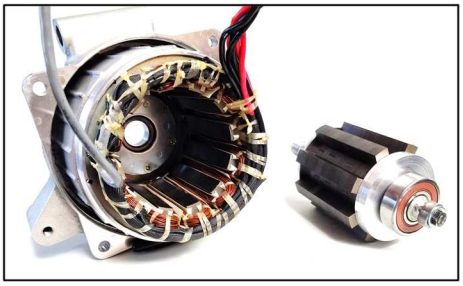

Fig. 13. Scaled SRM stator and rotor prior to assembly and installation with dynamometer.

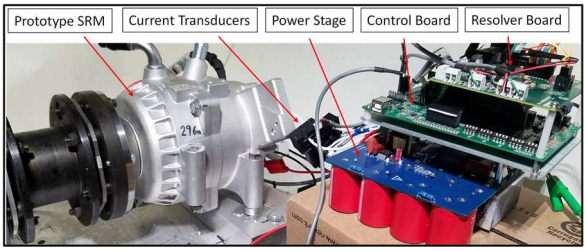

Fig. 14. SRM stator installed with dynamometer and power stage, control board, and resolver board.

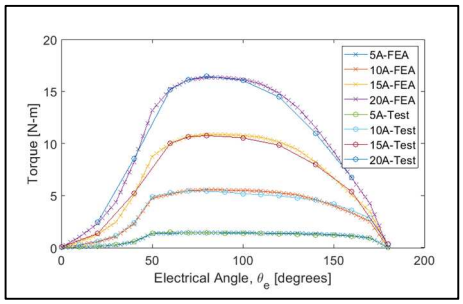

Fig. 15. Measured and simulated SRM single phase locked rotor torque versus electrical angle for various currents.

Locked rotor torque measurements were made by using a mechanism to lock the SRM rotor shaft at various positions as DC current was applied. Test results were about 2-5% lower than original FEA simulations depending on current level, and an increase of the airgap by ~0.1 mm in FEA simulations resulted in a close match with experiments, as shown in Fig. 15. Simulations were repeated with the new torque and flux-linkage mapping from 2D static FEA and torque-speed maps of efficiency, torque ripple, and control conditions were generated for the $k_{eff-ctrl}$ = 0 and 1 conditions.

In general, minimum torque ripple control conditions correlate with more overlap between phases with a lower peak current while maximum efficiency control conditions correlate with less overlap and higher current across positions with higher torque-per-ampere. Comparisons of simulated and

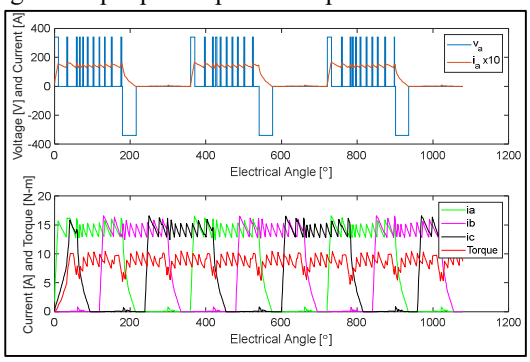

Fig. 16. Simulated SRM voltage, current, and torque at 1,000 rpm and 8 Nm with $k_{eff-ctrl}$ = 0.

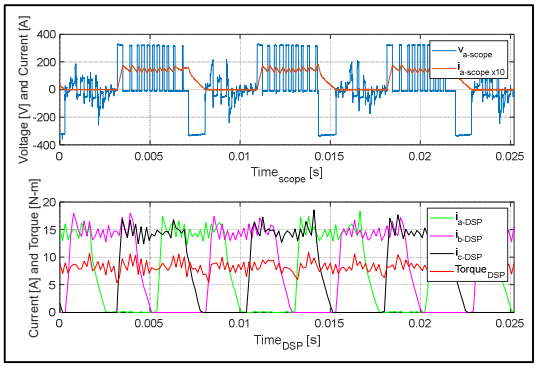

Fig. 17. Measured SRM voltage, current, and experimental torque at 1,000 rpm and 8 Nm with $k_{eff-ctrl}$ = 0.

measured voltage, current, and torque at 1,000 rpm and 8 Nm are provided in Figs. 16 and 17, respectively. Monitoring of the real time analog output of the torque transducer resulted in accurate average torque matching the OEM torque readout. However, torque ripple was much lower than predicted as most torque transducers are not intended to measure instantaneous torque. Therefore, the experimental instantaneous torque was approximated by interpolating the simulated three-phase locked rotor torque based on the measured three-phase currents and position.

Overall, simulated waveforms match closely with measured waveforms, and simulated and experimental torque ripple curves throughout the torque-speed range are provided in Figs. 18 and 19, respectively. Experimental torque ripple ranged from 8 to 15% higher than simulated torque ripple, and this discrepancy might be attributed to timing and switching characteristics of the DSP and power stage, instantaneous speed variation, and noise on the sampled current and position feedback. Simulated and measured efficiency contour maps are provided in Figs. 20 and 21, respectively, and close agreement can be observed throughout most of the torque-speed range. Discrepancies might be attributed to variations in winding temperature and loss predictions in simulation.

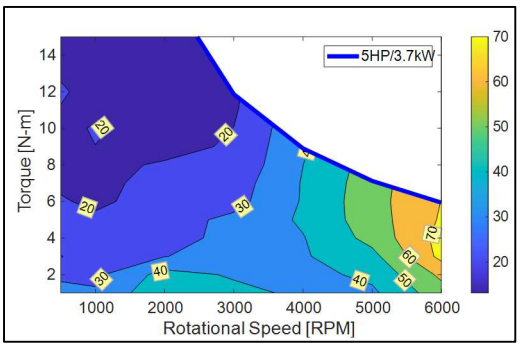

Fig. 18. Simulated SRM torque ripple contours with $k_{eff-ctrl}$ = 0.

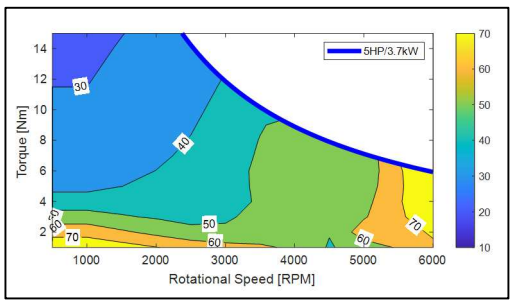

Fig. 19. Experimental SRM torque ripple contours with $k_{eff-ctrl}$ = 0.

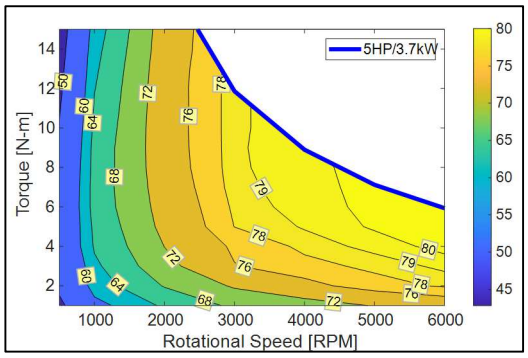

Fig. 20. Simulated SRM efficiency contours with $k_{eff-ctrl}$ = 1.

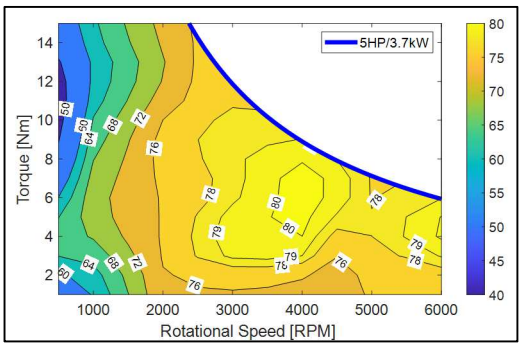

Fig. 21. Measured SRM efficiency contours with $k_{eff-ctrl}$ = 1.

VI. Conclusions and Future Work

A framework and method to perform systematic co-optimization of SRM design and control been proposed and demonstrated. Transient models rely on torque and flux-linkage lookup tables from 2D FEA to yield a decrease in computation time by a factor of at least 100 times in comparison with 2D transient FEA. This reduction in computational time greatly facilitates broad sweeps of both machine design and control parameters. Examples were provided regarding the establishment of performance functions for optimizing control conditions and overall machine geometry with respect to operational efficiency and torque ripple. Future work will include similar systematic assessments of the particle swarm optimization-based current profiling approach (proposed in [23]) to further minimize torque ripple. Other future work may include the incorporation of acoustic noise modeling and minimization, as well as parallelization of the modeling codes.

References

[1] T. J. E. Miller, "Optimal design of switched reluctance motors," *in IEEE Trans. Ind. Electronics*, vol. 49, no. 1, pp. 15-27, Feb. 2002.

[2] B. Mahadevan and K. Vijayarajan, "Evolutionary computation based multi-objective pole shape optimization of switched reluctance machine", *International Journal of Electrical Power & Energy Systems*, vol. 43, no. 1, pp. 63-69, Dec. 2012.

[3] D. Lee, T. H. Pham and J. Ahn, "Design and operation characteristics of four-two pole high-speed SRM for torque ripple reduction," *in IEEE Trans. Ind. Electronics*, vol. 60, no. 9, pp. 3637-3643, Sept. 2013.

[4] C. E. Carstensen, N. H. Fuengwarodsakul and R. W. de Doncker, "Flux linkage determination for correct modeling of switched reluctance machines - dynamic measurement versus static computation," *2007 IEEE International Electric Machines & Drives Conference*, Antalya, 2007, pp. 1317-1323.

[5] T. Burress and C. Ayers, "Development and experimental characterization of a multiple isolated flux path reluctance machine," *2012 IEEE Energy Conversion Congress and Exposition (ECCE)*, Raleigh, NC, 2012, pp. 899-905.

[6] M. Franke, O. Punk, M. Brutscheck and U. Schmucker, "Magnetic equivalent circuit modeling of rolling rotor switched reluctance motors," *33rd International Spring Seminar on Electronics Technology,* ISSE 2010, Warsaw, 2010, pp. 320-325.

[7] W. Peng and J. Gyselinck, "Combined magnetic-equivalent-circuit and finite-element modelling of switched reluctance machines," *2016 IEEE International Energy Conf. (ENERGYCON)*, Leuven, 2016, pp. 1-6.

[8] M. N. Anwar, I. Husain and A. V. Radun, "A comprehensive design methodology for switched reluctance machines," *in IEEE Trans. on Industry Applications*, vol. 37, no. 6, pp. 1684-1692, Nov.-Dec. 2001.

[9] P. Pramod, P. Nuli, R. Mitra and S. Mehta, "Modeling and simulation of switched reluctance machines for control and estimation tasks," *2019 IEEE International Electric Machines & Drives Conference (IEMDC)*, San Diego, CA, USA, 2019, pp. 565-570.

[10] M. Balaji and V. Kamaraj, "Design optimization of switched reluctance machine using particle swarm optimization," *2011 1st International Conference on Electrical Energy Systems*, Newport Beach, CA, 2011, pp. 164-169.

[11] C. Ma and L. Qu, "Multiobjective optimization of switched reluctance motors based on design of experiments and particle swarm optimization," *in IEEE Transactions on Energy Conversion*, vol. 30, no. 3, pp. 1144-1153, Sept. 2015.

[12] H. Yahia, N. Liouane, R. Dhifaoui "Multiobjective differential evolution-based performance optimization for switched reluctance motor drives", Turkish Journal of Electrical Engineering and Computer Science, vol. 21, no. 4, 2013, pp. 1061-1076

[13] S. Li, S. Zhang, T. G. Habetler and R. G. Harley, "Modeling, design optimization, and applications of switched reluctance machines—a review," *in IEEE Transactions on Industry Applications*, vol. 55, no. 3, pp. 2660-2681, May-June 2019.

[14] N. T. Shaked and R. Rabinovici, "New procedures for minimizing the torque ripple in switched reluctance motors by optimizing the phase-current profile," *in IEEE Transactions on Magnetics*, vol. 41, no. 3, pp. 1184-1192, March 2005.

[15] H. Makino, T. Kosaka and N. Matsui, "Control performance comparisons among three types of instantaneous current profiling technique for SR motor," *7th IET Intl. Conf. on Power Electronics, Machines and Drives (PEMD 2014)*, Manchester, 2014, pp. 1-6.

[16] C. Ma, L. Qu, R. Mitra, P. Pramod and R. Islam, "Vibration and torque ripple reduction of switched reluctance motors through current profile optimization," *2016 IEEE Applied Power Electronics Conference and Exposition (APEC)*, Long Beach, CA, 2016, pp. 3279-3285.

[17] Y. Wei, M. Qishuang, Z. Poming and G. Yangyang, "Torque ripple reduction in switched reluctance motor using a novel torque sharing function," *2016 IEEE International Conference on Aircraft Utility Systems (AUS)*, Beijing, 2016, pp. 177-182.

[18] N. Sahoo, S. Panda, and P. Dash, "A current modulation scheme for direct torque control of switched reluctance motor using fuzzy logic," *Mechatronics*, vol. 10, no. 3, pp. 353-370, April 2000.

[19] M. Divandari, R. Brazamini, A. Dadpour and M. Jazaeri, "A novel dynamic observer and torque ripple minimization via fuzzy logic for SRM drives," *2009 IEEE International Symposium on Industrial Electronics*, Seoul, 2009, pp. 847-852.

[20] J. A. Domínguez-Navarro, J. S. Artal-Sevil, H. A. Pascual and J. L. Bernal-Agustín, "Fuzzy-logic strategy control for switched reluctance machine," *2018 Thirteenth Intl. Conf. on Ecological Vehicles and Renewable Energies (EVER)*, Monte Carlo, Monaco, 2018, pp. 1-5.

[21] S. Wang, F. Liu and J. Chou, "Design on sliding mode controller with adaptive fuzzy compensation for switched reluctance motor drive systems," *2016 International Symposium on Computer, Consumer and Control (IS3C)*, Xi'an, 2016, pp. 239-242.

[22] T. Burress and L. M. Tolbert, "A framework for multiple objective co-optimization of switched reluctance machine design and control," *2021 IEEE Transportation Electrification Conference & Expo (ITEC)*, Chicago, IL, USA, 2021, pp. 1-6.

[23] T. Burress, "Benchmarking State-of-the-Art Technologies," 2013 U.S. DOE Hydrogen and Fuel Cells Program and Vehicle Technologies Program Annual Merit Review and Peer Evaluation Meeting, May 14th, 2013.

[24] J. Gieras, *Advancements in Electric Machines*, Springer London Limited, 2008.

[25] D. Lin, P. Zhou, W. N. Fu, Z. Badics and Z. J. Cendes, "A dynamic core loss model for soft ferromagnetic and power ferrite materials in transient finite element analysis," in *IEEE Transactions on Magnetics*, vol. 40, no. 2, pp. 1318-1321, March 2004.